Variable-Temperature Noise Characterization of N-MOSFETs Using an In-Situ Broadband Amplifier

Kenji Ohmori, *Member, IEEE*, and Shuhei Amakawa, *Member, IEEE*

***Abstract*—Characterization of broadband noise of MOSFETs from room temperature down to 120 K in fine temperature steps is presented. A MOSFET is mounted on a reusable printed circuit board vehicle with a built-in low-noise amplifier, and the vehicle is loaded into a cryogenic chamber. The vehicle allows noise measurement in the frequency range from 50 kHz to 100 MHz. At low frequencies, it enables extraction of activation energies associated with electron trapping sites. At high frequencies, as has been suggested by noise figure measurements, the white noise of MOSFETs is shown to be dominated by the shot noise, which has much weaker temperature dependence than the thermal noise. The shot noise will be a problematic noise source in broadband RF CMOS circuits operating at cryogenic temperatures.**

***Index Terms*—cryogenic CMOS, white noise, 1/f noise, low-frequency noise spectroscopy, device modeling, quantum computing**

I. Introduction

Low temperature environment enhances performance of CMOS devices through the improvement of the carrier mobility, subthreshold slope, Cu wire resistance, and thermal noise [1-3]. Applications of "cold" CMOS range from high-performance computing to space exploration and low temperature physics. Quantum computing is one of the challenging technologies that require that the power of CMOS circuits be made available at cryogenic temperatures. To maintain the coherence time of quantum bits (qubits), such as superconductive qubits [4-6] and semiconductor spin qubits [7], a quantum processor comprising several to several tens of qubits is located in a sub-decikelvin cryogenic chamber. At present, peripheral circuits for controlling the quantum processor typically operate at room temperature and are connected to the quantum processor via long RF cables. However, as the number of qubits increases exponentially in the near future, error correction needs to be implemented for maintaining the computation fidelity over the coherence time of qubits. Then, the control latency will be critical for continuous operation of such a quantum processor [8-11]. Efforts have been made to move low-power RF CMOS controllers into a few-kelvin chamber that encloses the sub-decikelvin chamber [10].

For the design of high-performance cryogenic RF CMOS circuits for whatever purposes, MOSFET compact models valid down to cryogenic temperatures are necessary [12-13]. At cryogenic temperatures, many performance parameters including the saturation value of the drain current (I_d) and electron mobility improve and, in addition, peculiar phenomena, such as bandgap widening, carrier freeze-out, and self-biasing, appear [14]. Therefore, continuous characterization of MOSFETs at varying temperatures starting from room temperature down to cryogenic temperatures is important for developing physics-based predictive device models. In particular, wideband noise modeling is essential for the development of low-noise circuits.

MOSFETs are known to exhibit flicker noise at low frequencies and white noise at high frequencies. Physical origins of flicker noise and white noise are different, and their power spectral densities are independent of each other. White noise can be further classified into thermal noise and shot noise. These are not completely independent of each other and become indistinguishable under a zero drain bias [15,16]. When a nonzero drain bias is applied, the shot noise becomes dominant [17,18]. White noise from a local oscillator have recently been shown to adversely affect the operation of wideband millimeter-wave circuits [19,20].

The noise figure (NF) measurement is typically used to characterize the white noise of MOSFETs [21,22]. The most commonly used Y-factor method of NF measurement requires a hot noise source. In cryogenic environments, this method is not straightforwardly applicable because cryogenic noise sources are not commercially available [23]. Therefore, either the cold-source method or the cold-attenuator method [24] is employed, in which several cooling cycles per characterizing a single device under test (DUT) are required for complicated calibration [25]. On the other hand, the maximum measurable frequency of low-frequency noise measurement systems is usually too low to cover white noise due to parasitic capacitance inherent in such systems.

A proof-of-concept noise probe for on-wafer broadband noise characterization was demonstrated at room temperature, achieving noise measurement from 100 kHz up to 800 MHz [26,27]. This approach "quietly" listens to noise from a DUT as does a conventional low-frequency noise measurement system, and therefore does not require a hot noise source. This was made possible by reducing the parasitic capacitance by placing a broadband low-noise amplifier (LNA) in the probe itself. At present, an improved version of the noise probe is commercially available [28], details of which were presented in [18]. In this study, we apply the same principle to

The authors are with Device Lab Inc., ILC Bldg., Tennodai 1-1-1, Tsukuba, Ibaraki 305-8577, Japan (e-mail: ohmori@devicelab.co.jp).

the development of an in-situ system for variable-temperature broadband noise measurements down to 120 K [29].

Low-frequency noise from a very small MOSFET can reveal individual trapping/detrapping of a single electron to/from a trapping site. Using this capability, low-frequency noise measurement is commonly employed to characterize the quality of gate dielectrics [30]. In this paper, we will also demonstrate low-frequency noise spectroscopy (LFNS) [31-34], in which, by characterizing temperature-dependent noise intensities of a MOSFET, the activation energy related to electron trapping is extracted.

We will also look at the temperature dependence of white noise, especially shot noise, and the suppression of the latter compared to its theoretical maximum value (full shot noise), through the use of the so-called Fano factor or the shot-noise suppression factor.

II. Experimental Setup and Measurement

We developed a reusable printed circuit board (PCB) vehicle for cryogenic measurements, on which a DUT is mounted. Also on the PCB vehicle is a broadband LNA capable of covering 50 kHz to 100 MHz for in-situ sensing of noise from the DUT. The lowest frequency is limited by the presence a dc-block capacitor at the LNA input. A DUT is mounted on the vehicle right next to the LNA. The configuration of electrical instruments is similar to that in [18], except that the PCB vehicle is placed in a cryogenic helium chamber as schematically shown in Fig. 1. The length of the cables in the cryogenic chamber is about 1 m. We characterized the LNA and intervening structures, including the cables, connectors, and parasitics associated with the PCB vehicle, at every kelvin from 300 to 120 K by extensive measurements. Use was also made of some dummy PCB vehicles without a DUT and a method of de-embedding, commonly employed at microwave frequencies. The noise generated by the broadband LNA and effects of parasitics are then calibrated out by using the data thus obtained [18]. Note that once the variable-temperature calibration of a vehicle is completed through several cooling cycles, measurements of dc and noise characteristics can be conducted in a single cooling cycle.

We employed a semiconductor device analyzer (B1500A, Agilent Technologies), equipped with four high-resolution source-measure units (HR-SMUs), for biasing the DUT, and a spectrum analyzer (N9030A, Agilent Technologies) for reading the output from the LNA. The noise generated by the spectrum analyzer is accounted for, in effect, by turning on its Noise Floor Extension option [35]. Custom-built low-pass filters were used to filter out noise from the HR-SMUs.

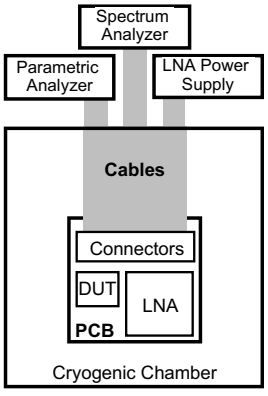

Fig. 1. Schematic of a cryogenic system with a PCB vehicle for wideband noise measurement.

We characterized N-MOSFETs from a few different semiconductor foundries. Measurement data of three types of MOSFETs, fabricated by using three different process technologies and denoted by type-A/B/C, will be examined. The gate lengths and widths (L/W) of type-A, B, and C MOSFETs are 240 nm/2.5 μm, 120 nm/10 μm, and 120 nm/2.5 μm, respectively. Each of the DUTs had 4 contact pads (gate, drain, source, and substrate electrodes) and was mounted on a PCB vehicle by flip-chip (type-A/C DUTs) or wire bonding (type-B DUT) for stable measurements at different temperatures. If one uses a cryogenic probe station, the probe tips shrink in length as T decreases, which makes stable continuous variable-T measurement very difficult. Therefore, it is beneficial also in this regard to bond a DUT next to an LNA.

DUT temperatures were measured using a silicon diode sensor attached next to the DUT on the PCB vehicle. The temperature ranges examined are from 5 to 300 K for dc I-V measurements and 120 to 300 K for noise measurements. The lowest temperature of 120 K of the noise measurement was dictated by the carrier freeze-out of bipolar transistors in the LNA.

III. Variable-Temperature Characterization

A. Dc Characteristics

Figure 2(a) shows I_d-V_g curves at $T = 5$ to 300 K for a type-A DUT under a drain-source voltage, V_d, of 0.05 V. The I_d-V_g measurement was carried out at every 1–5 K step. At low temperatures, I_d decreases in the low-V_d region and increases in the high-V_d region. The change in the transconductance g_m is shown in Fig. 2(b). The dependence of the threshold voltage V_th on T is plotted in Fig. 3(a). V_th was extracted by drawing a tangential line on an I_d-V_g curve at the point where g_m assumes a maximum value. V_th shifts from 0.74 V at 300 K to 0.94 V at 5 K. The electron current density is expressed as

$$\boldsymbol{J}_\mathrm{n} = qn\mu_\mathrm{n}\boldsymbol{\mathcal{E}} + qD_\mathrm{n}\nabla n, \qquad (1)$$

where n is the concentration of electrons in the inversion layer, μ_n is the electron mobility, $\boldsymbol{\mathcal{E}}$ is the electric field, and D_n is the diffusion coefficient, which is proportional to T. The diffusion-current component of I_d decreases as the temperature becomes lower, resulting in higher V_th [Fig. 3(a)] and steeper subthreshold slope [Fig. 2(a)]. Figure 3(b) shows $(g_\mathrm{m}/I_\mathrm{d})^2T$ versus T for $V_\mathrm{d} = 0.05$ V and 1.0 V. The ratio $g_\mathrm{m}/I_\mathrm{d}$ is the normalized (per-unit-drain-current) transconductance, often examined in relation to surface potential fluctuations [36,37]. The peak g_m values in Fig. 2(a) and the corresponding I_d were used to estimate $(g_\mathrm{m}/I_\mathrm{d})^2T$ for $V_\mathrm{d} = 0.05$ V (open squares) in

Fig. 3(b), while for $V_d = 1.0$ V (open circles), g_m and I_d values at $V_g = 1.5$ V were used because g_m-V_g curves (not shown) exhibited monotonic increase at $V_d < 1.5$ V. $(g_m/I_d)^2T$ is to be considered later in Section III.B in connection with the dependence of normalized noise intensity on T.

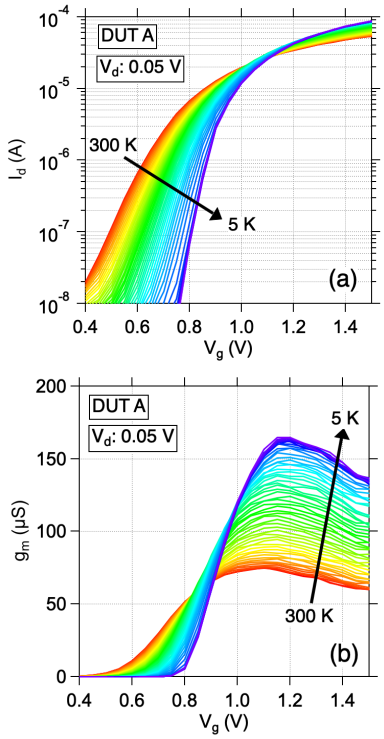

Fig. 2. (a) Typical MOSFET I_d - V_g characteristics and (b) transconductance g_m at temperatures ranging from 5 to 300 K.

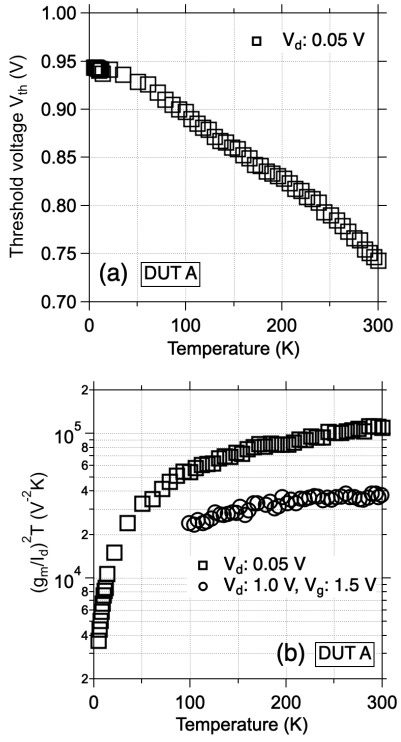

Fig. 3. (a) Threshold voltage V_{th} versus T for $V_d = 0.05$ V. (b) $(g_m/I_d)^2T$ versus T for $V_d = 0.05$ and 1.0 V.

Figure 4 shows I_d-V_d curves at $T = 122$ to 300 K for a type-A DUT under (a) $V_g = 0.9$ and (b) 1.5 V. I_d in Fig. 4(a) decreases as T decreases, whereas I_d in Fig. 4(b) increases, consistent with the behavior observed in Fig. 2(a). The dependence of I_d on T under a given bias condition is affected by many factors including the process technology node, the structure of the MOSFET, and the impurity concentration [2]. Therefore, continuous variable-temperature characterization is necessary for physics-based predictive device modeling.

B. 1/f Noise in the Saturation Region

Before focusing on white noise, we demonstrate a measurement result using the vehicle in the low-frequency, flicker-noise region. Changes in drain-current noise power spectral density S_{Id} for a type-A DUT are shown in Fig. 5(a,b). The bias conditions are (a) $V_g = 0.9$ and (b) 1.5 V with $V_d = 1.0$ V in both cases. The corresponding I_d values can be found in Fig. 4. S_{Id} normalized by I_d^2 for selected temperatures is shown in Fig. 5(c,d). $1/f^\beta$ frequency dependence is observed with β gradually decreasing in the high-frequency region above 10 MHz, where $-\beta$ is the slope of the noise power spectrum on a log-log plot. The average β value for $V_g = 0.9$ V, extracted in the frequency range from 100 kHz to 1 MHz, decreases from 1.07 at 300 K to 0.77 at 122 K. As shown in Fig. 3(a), V_{th} is a decreasing function of temperature. We used the gate-source voltage, V_g, as biasing points in variable-temperature noise measurements. Under the condition of $V_g = 0.9$ V, the channel is in strong inversion, and the gate overdrive voltage $V_g - V_{th}$ decreases as T decreases. The values of $V_g - V_{th}$ in Fig. 5(a) are

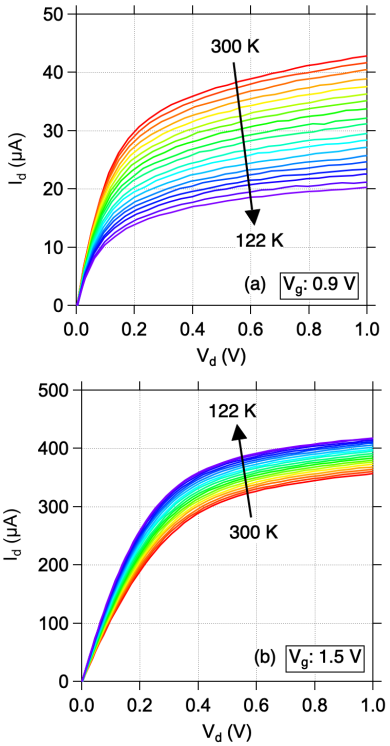

Fig. 4. I_d-V_d curves for (a) $V_g = 0.9$ V and (b) 1.5 V.

0.16 and 0.03 V at 300 and 120 K, respectively. Trapping rate of electrons is proportional to $\exp[-(E_c - E_t)/k_B T]$, where E_c is the bottom energy of the conduction band, and E_t is the trap level, and, therefore, is strongly affected by T [38]. The change in β for $V_g = 0.9$ V in Fig. 5(a) could be related to a depth- and E_t-dependent trap profile in the oxide layer [39, 40]. The magnitudes of normalized S_{Id} for 122 and 300 K intersect in Fig. 5(c) and the inequality is reversed at 400 kHz. As $V_g - V_{th}$ increases, the intensity of normalized S_{Id} decreases [41]. Therefore, the intersection frequency should be higher if a comparison is made under the same gate overdrive voltage. Studies on low frequency noise are typically conducted in a frequency range from 1 Hz to 10 kHz, or at most 100 kHz. It does appear very important that the measurement frequency range is significantly extended when trying to develop predictive device noise models valid in various operating conditions, including low temperatures.

On the other hand, the values of β do not change very much when $V_g = 1.5$ V and $V_d = 1.0$ V as shown in Fig. 5(b,d). Although I_d increases as T decreases [Fig. 4(b)], S_{Id} (and obviously, normalized S_{Id}) decrease. The relationship between the normalized S_{Id} and $(g_m/I_d)^2$ is expressed as [37]

$$\frac{S_{Id}}{I_d^2} = \left(\frac{g_m}{I_d}\right)^2 \frac{q^2 \rho \lambda k_B T}{C_{ox} W L f}, \qquad (2)$$

where ρ is the density of the McWhorter states in the oxide, λ is the electron wave penetration depth in the oxide, k_B is the Boltzmann constant, C_{ox} is the capacitance of the oxide per unit area, and W is the gate width. $(g_m/I_d)^2 T$, shown in Fig. 3(b), for the same bias condition also decreases as T decreases. This is consistent with the slight decrease in normalized S_{Id} in the low-frequency region in Fig. 5(d). To provide a perspective, the temperature dependence of flicker noise in the measured temperature range ($T \geq 122$ K) is relatively weak, consistent with Fig. 3(b). But further study is needed to provide a more general perspective covering lower temperatures.

C. *Low-Frequency Noise Spectroscopy (LFNS)*

Next, we conduct an analysis of the physical origin of the observed low-frequency noise. Trapping and detrapping of electrons, typically at the interface between the gate dielectric film and the channel of a MOSFET, result in random telegraph noise (RTN) in the time domain [42]. This is often observed as waveforms exhibiting two discrete levels with a certain time constant τ of transition between the two levels, corresponding to capture and emission of an electron. In the frequency domain, RTN appears as a Lorentzian-shaped hump at a characteristic frequency $f_\tau \approx (2\pi\tau)^{-1}$ [42]. Figure 6 shows changes in drain-current noise power spectral density S_{Id} for a type-B DUT at different temperatures. Note that the effects of parasitics associated with the PCB were calibrated out as explained in Section II, but those associated with stud bumps (for flip-chip bonding) and bond wires were not. Since the type-B MOSFET was wire-bonded and bond wires have larger parasitics than stud bumps, the maximum frequency shown in Fig. 6 is 50 MHz (versus 100 MHz in Fig. 5 for type-A). S_{Id} exhibits Lorentzian behavior with temperature-dependent f_τ. Since the time constant is a function of the activation energy and T, the frequency f_τ shifts to higher frequencies as T rises. Figure 7(a) shows S_{Id} versus temperature extracted at frequencies ranging from 50 kHz to 5 MHz. Two sets of peaks, labeled "Peak 1" and "Peak 2," were observed. The peak temperatures depend on the

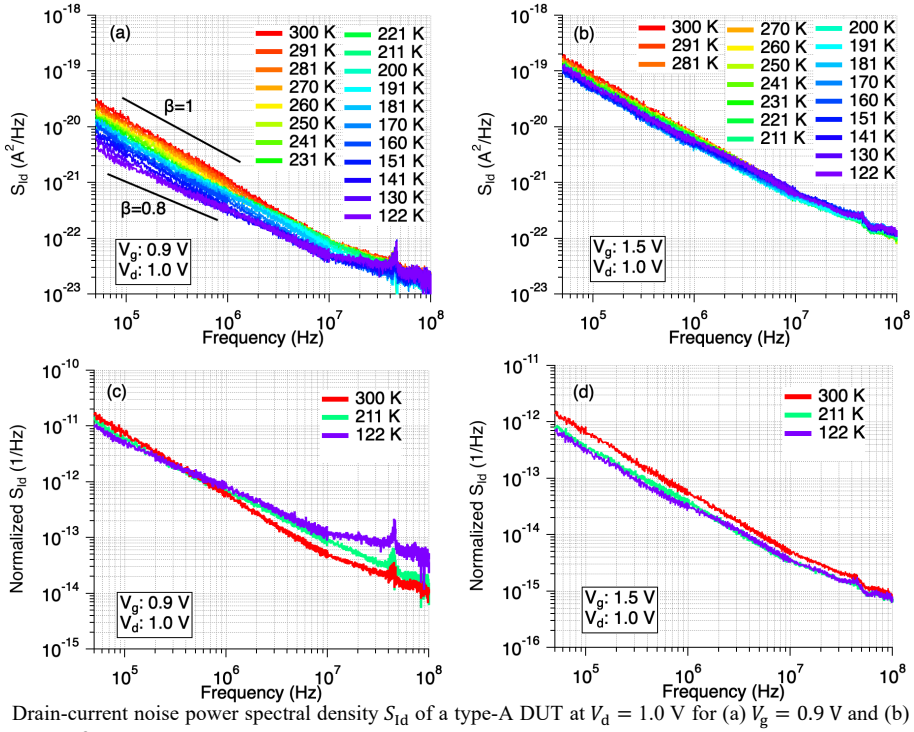

Fig. 5. Drain-current noise power spectral density S_{Id} of a type-A DUT at $V_d = 1.0$ V for (a) $V_g = 0.9$ V and (b) 1.5 V. S_{Id} normalized by I_d^2 for (c) $V_g = 0.9$ V and (d) 1.5 V.

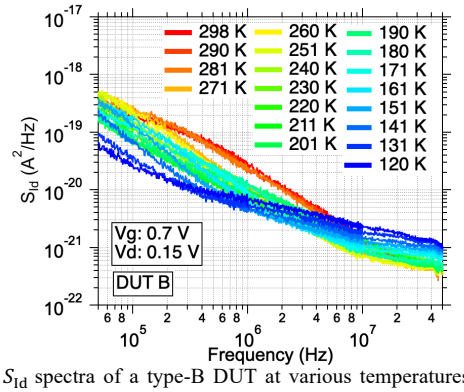

Fig. 6. S_{Id} spectra of a type-B DUT at various temperatures, showing wavy curves resulting from RTN.

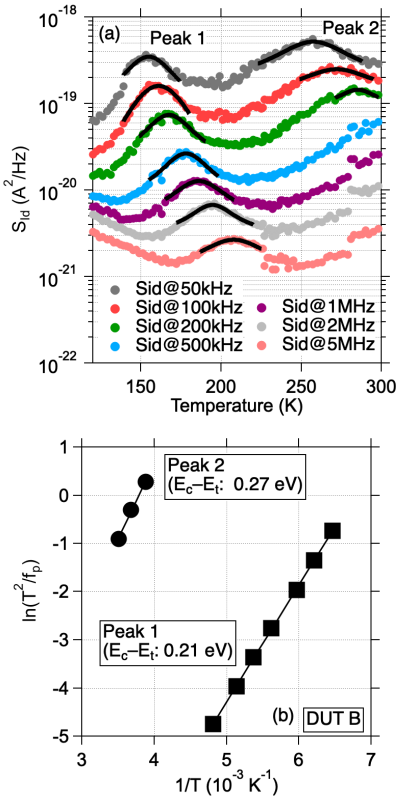

Fig. 7. (a) Low-frequency noise spectroscopy for a type-B DUT. Two sets peaks were observed. (b) Arrhenius plots for extracting activation energies. f_p denotes a frequency of S_{Id}(T) used for evaluation of the peak temperature in (a).

frequency. For an electron trap in a MOSFET, the relationship between T and f is expressed as [31]

$$\ln\left(\frac{T^2}{f}\right) = \frac{E_{\mathrm{c}}-E_{\mathrm{t}}}{k_{\mathrm{B}}T} + C, \qquad (3)$$

where C is a constant that includes the capture cross section of the trap and the electron effective mass. This allows us to use the Arrhenius method of estimating the activation energy $E_{\mathrm{c}} - E_{\mathrm{t}}$. Figure 7(b) shows an Arrhenius plot for the peak temperatures and frequencies extracted from Fig. 7(a). The values of $E_{\mathrm{c}} - E_{\mathrm{t}}$ were found to be 0.21 and 0.27 eV for "Peak 1" and "Peak 2," respectively. Identification of trap species, for example, hydrogen, interstitial carbon, and interstitial boron, was reported [33], in which the activation energies ranged from 0.10 to 0.44 eV. To do the same here, further investigation using more DUTs will be required.

In quantum computing, a major cause of decoherence is noise, which is often generated by defects and traps in close proximity to qubits [43]. LFNS is applicable to systems in which current or voltage is affected by trapping phenomena [32]. LFNS could also be employed for studies of improving the coherence time of qubits.

D. Pure Thermal Noise at Zero Drain Voltage

What is unique about using the vehicle with the built-in broadband LNA is the capability to characterize white noise, depending on the bias condition. Figure 8 shows S_{Id} versus frequency under zero-drain-bias ($V_{\mathrm{d}} = 0$ V) conditions with V_{g} from 0.8 to 1.6 V at (a) $T = 300$ and (b) 121 K. The frequency range is from 50 kHz to 100 MHz. Note that the maximum measurable frequency in commercially available low-frequency noise systems is a few tens of MHz at the highest. The observed white noise in Fig. 8 can be regarded either as thermal noise, given by $4k_{\mathrm{B}}T/R_{\mathrm{dif}}$, where $R_{\mathrm{dif}} = \partial V_{\mathrm{d}}/\partial I_{\mathrm{d}}$, or as shot noise [44]. As V_{g} increases, R_{dif} decreases, resulting in higher white noise levels.

Noise measurements were conducted continuously from 120 to 300 K. In Fig. 9, temperature dependence of extracted S_{Id} values at 10 MHz for (a) $V_{\mathrm{g}} = 1.0$ V and (b) V_{g} ranging from 0.8 to 1.6 V are plotted as a function of the theoretical thermal noise intensity S_{th} ($= 4k_{\mathrm{B}}T/R_{\mathrm{dif}}$). As the temperature becomes low, S_{th} and hence S_{Id} decrease. We observed a good linear relationship between S_{th} and S_{Id} with a slope of unity. The

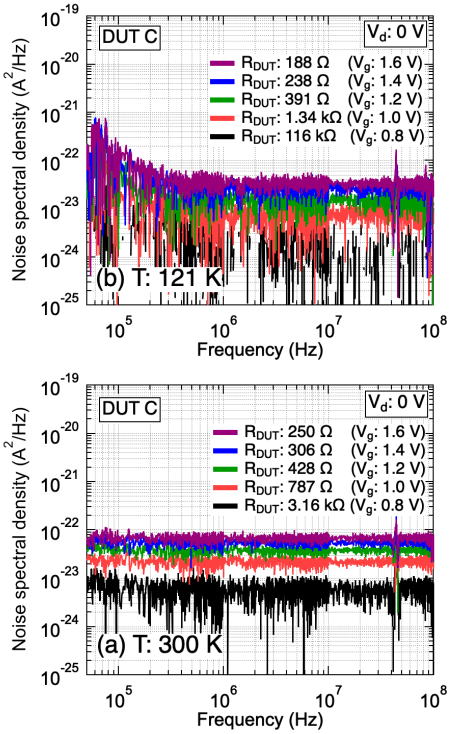

Fig. 8. Noise power spectral density S_{Id} of a type-C DUT obtained at $V_{\mathrm{d}} = 0$ V and at (a) $T = 300$ and (b) 121 K. Under the same bias condition, the white noise level at $T = 121$ K is lower than that at $T = 300$ K.

range of the linear relationship in Fig. 9(b) is from 4×10^{-25} to 7×10^{-23} A^2/Hz, which corresponds to $R_{\rm dif}$ values from 23 kΩ to 188 Ω. This result also indicates that the calibration of the LNA is successful over the ranges of frequencies and temperatures demonstrated in Figs. 8–9.

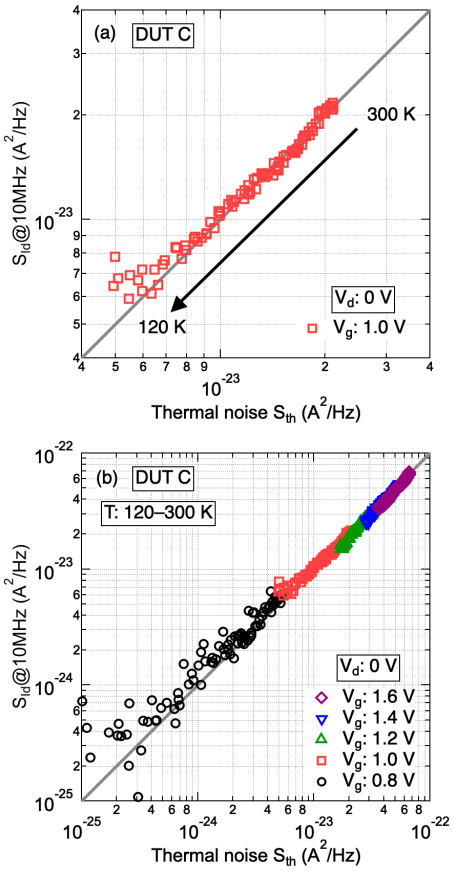

Fig. 9. (a) Change in $S_{\rm Id}$ of a type-C DUT extracted at 10 MHz versus the theoretical thermal noise ($4k_{\rm B}T/R_{\rm dif}$) with T ranging from 300 to 120 K. The gate voltages $V_{\rm g}$ are (a) 1.0 V and (b) 0.8, 1.0, 1.2, 1.4, 1.6 V.

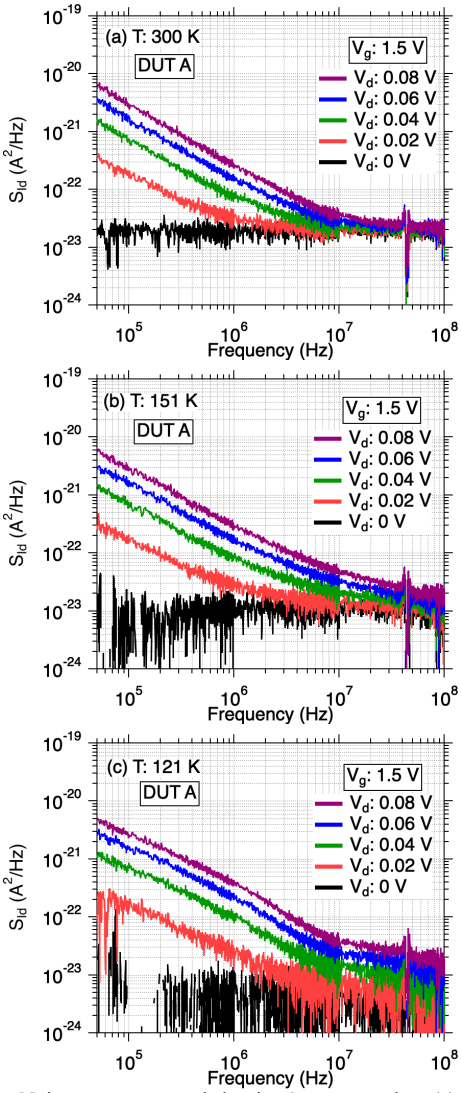

Fig. 10. Noise power spectral density $S_{\rm Id}$ measured at (a) T =300 K, (b) 151 K, and (c) 121 K.

E. Shot-Noise Evaluation in the Linear Region

When a nonzero $V_{\rm d}$ is applied, $I_{\rm d}$ starts to increase and shot noise component that cannot be regarded as thermal noise emerges. In order to characterize white noise that consists of thermal and shot noise, noise measurement was conducted in the linear region of MOSFET operation using the type-A DUT, which showed the lowest levels of flicker noise. Figure 10 shows $S_{\rm Id}$ for $V_{\rm g} = 1.5$ V and $V_{\rm d} = 0$, 0.02, 0.04, 0.06, and 0.08 V at (a) $T = 300$, (b) 151, and (c) 121 K. Transitions from flicker noise dominance at low frequencies to white noise dominance at high frequencies are clearly observed. Although the slope of $S_{\rm Id}(f)$ becomes very small at high frequencies, the slope at large $V_{\rm d}$ values is not quite zero. $S_{\rm Id}(f)$ above 1 MHz can be regarded as the sum of white noise and residual flicker noise. We therefore estimated the level of white noise, $S_{\rm w}$, and the corner frequency, $f_{\rm c}$, at which the intensity of flicker noise is equal to that of white noise, by using [18]

$$S_{\rm Id}(f) = K_{\rm f}/f^{\beta} + S_{\rm w}, \qquad (4)$$

where $K_{\rm f}$ is the value of $S_{\rm Id}(f)$ when $f = 1$ Hz, at which $S_{\rm w}$ is usually negligible ($K_{\rm f} \gg S_{\rm w}$). The corner frequency is given by $f_{\rm c} = (K_{\rm f}/S_{\rm w})^{1/\beta}$. Here, a value of β averaged over 300 kHz to 1 MHz and $S_{\rm Id}$ values at 10 and 30 MHz at each T were used to estimate $S_{\rm w}$ and $K_{\rm f}$. A straight $1/f^{\beta}$ line on a log-log $S_{\rm Id}$-versus-f plot is assumed in (4). The accuracy of extraction of $S_{\rm w}$ by using (4) is affected by humps due to RTN. For example, this is observed as a broad hump in $S_{\rm Id}$ (around 1 MHz) in Fig. 10(c). Hereafter, we will limit the lowest temperature analyzed by using (4) to 150 K because flicker noise below 150 K does not exhibit a good straight $1/f^{\beta}$ line due to the appearance of RTN. As shown in Fig. 11, the corner frequency $f_{\rm c}$ gradually increases as T decreases mainly because the intensity of thermal noise decreases. $f_{\rm c}$ is higher for larger $V_{\rm d}$ due to higher flicker noise intensity.

Figure 12 shows the dependence of measured $S_{\rm Id}$ and the estimated white noise $S_{\rm w}$ on $V_{\rm d}$ for (a) $T = 300$ and (b) 151 K. Open circles/squares and solid squares show measured $S_{\rm Id}$ at 10/30 MHz and estimated $S_{\rm w}$ from (4), respectively. The difference between these values grows as $V_{\rm d}$ increases,

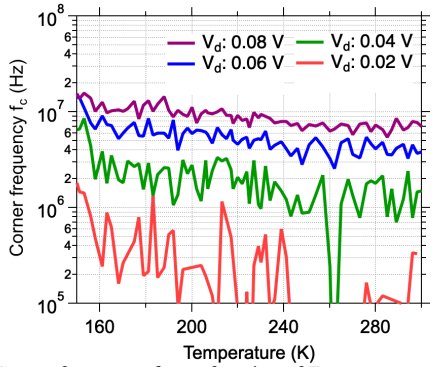

Fig. 11. Corner frequency f_c as a function of T.

resulting from the increase in residual flicker noise (Fig. 10). Thermal noise intensity $S_{\rm th}$ for nonzero-drain-bias conditions is given by [44]

$$S_{\rm th}(V_{\rm d}) = \frac{4k_{\rm B}TR_{\rm ch}(V_{\rm d})}{[R_{\rm dif}(V_{\rm d})]^2}, \tag{5}$$

where $R_{\rm ch} = V_{\rm d}/I_{\rm d}$ is the chord resistance [46]. Note that $R_{\rm ch}(V_{\rm d}) \neq R_{\rm dif}(V_{\rm d})$ unless $V_{\rm d} = 0$ V.

Also plotted in Fig. 12 are the expected thermal noise $S_{\rm th}$ (green dotted line) from (5), full shot noise $2qI_{\rm d}$ (orange solid line), and the sum of these (blue dot-dashed line). At $V_{\rm d} = 0$ V, $S_{\rm w}$ equals $S_{\rm th}$ and, as $V_{\rm d}$ increases, $S_{\rm w}$ increases along but below $2qI_{\rm d}$ [18]. The latter gives the maximum possible value of shot noise intensity, realized when statistical fluctuation of the carrier number is at its maximum. Here we introduce the crossover drain voltage $V_{\rm d,cross}$, at which $S_{\rm th}(V_{\rm d,cross}) = 2qI_{\rm d}$.

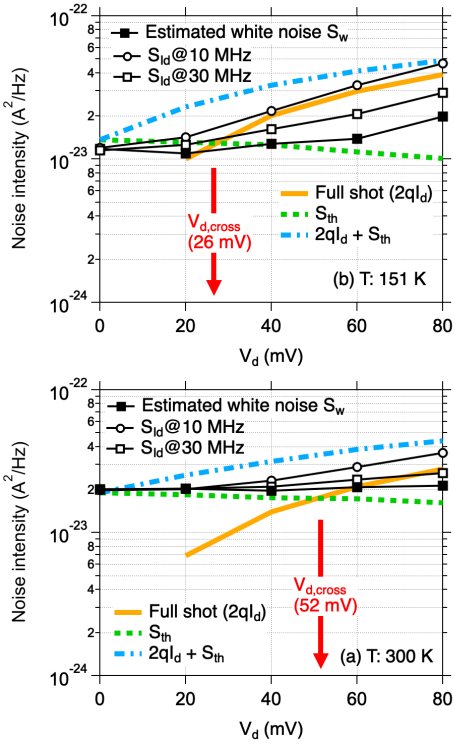

Fig. 12. Dependence of $S_{\rm Id}$ extracted at 10 and 30 MHz, and estimated white noise $S_{\rm w}$ on $V_{\rm d}$ at $V_{\rm g}$=1.5 V at (a) T =300 and (b) 151 K.

It follows from this equation that

$$\frac{2k_{\rm B}T}{q} = I_{\rm d}\frac{[R_{\rm dif}(V_{\rm d,cross})]^2}{R_{\rm ch}(V_{\rm d,cross})} \approx V_{\rm d,cross}, \tag{6}$$

because in the beginning of the linear region, $R_{\rm dif} \approx R_{\rm ch}$. Therefore, thermal noise $S_{\rm th}$ dominates under low drain bias ($V_{\rm d} \lesssim 2k_{\rm B}T/q$) and shot noise becomes dominant when $V_{\rm d} \gtrsim 2k_{\rm B}T/q$, as delineated by the red arrows in Fig. 12. The values of $2k_{\rm B}T/q$ for T = 300 and 151 K are 52 and 26 mK, respectively. Therefore, as clearly observed in Fig. 12, the onset drain voltage of shot noise predominance at low temperature is smaller than that at room temperature.

Figure 13 shows the relation between the estimated white noise $S_{\rm w}$ and the thermal noise $S_{\rm th}$ at $150 \leq T \leq 300$ K. Although temperatures are not explicitly shown in Fig. 13, decrease in the value of $S_{\rm th}$ (horizontal axis) for each $V_{\rm d}$ corresponds to lowering of T. As T decreases, $S_{\rm w}$ at $V_{\rm d} = 0$ V (black open squares) decreases, exhibiting a linear relationship with a nearly unity slope as was also seen in Fig. 9. In contrast, $S_{\rm w}$ (vertical axis) at $V_{\rm d} > 0$ V remains higher than the thermal noise $S_{\rm th}$, clearly demonstrating that shot noise becomes predominant at low temperatures. Shot noise originates from the discrete nature of carrier transport. In MOSFETs, the shot noise is considered to originate primarily from carriers crossing the potential barrier near the source [17,47], and secondarily from quasi-ballistic transport in the pinch-off region, where the inversion carrier density is low [48]. In this experiment, the observed shot noise should have resulted from the former because of the small values of $V_{\rm d}$.

When the charge of carriers that have crossed a barrier is not completely canceled by, say, background ions of opposite polarity, the space charge serves to regulate the barrier-crossing events somewhat. The current is then described as being "space-charge-limited" [44,45]. Shot noise intensity in such a situation tends to be smaller than that without space-charge limiting. Shot noise is often characterized by using the so-called Fano factor (or noise suppression factor) $F(\leq 1)$, given by the actual shot noise intensity divided by $2qI_{\rm d}$ [40,45,49]. Successful use of F for white noise modeling has been

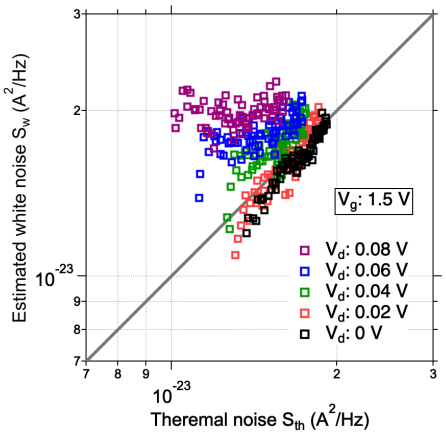

Fig. 13. Relation between the estimated white noise $S_{\rm w}$ and the thermal noise $S_{\rm th}$ at $V_{\rm d}$ ranging from 0 to 0.08 V.

demonstrated for short-channel MOSFETs [50]. A useful expression for measurement-based evaluation of F applicable even near and at $V_\mathrm{d} = 0$ V, where thermal noise and shot noise become indistinguishable, is [18]

$$F = \frac{S_\mathrm{W}}{2qI_\mathrm{d}+S_\mathrm{th}}. \quad (7)$$

Figure 14 shows temperature dependence of F for V_d ranging from 0 to 0.08 V. The black line in Fig. 14 is roughly equal to unity, which is the theoretically expected value of F at $V_\mathrm{d} = 0$ V. At room temperature, as V_d is raised from 0 V, F quickly falls in the linear region of MOSFET operation and becomes constant in the saturation region [18,50]. In this study, only the beginning of the linear region has been examined because of high f_c at larger values of V_d (Fig. 11). It is noteworthy that, in the linear region with V_d from 0.02 to 0.08 V, F slightly decreases as T decreases (Fig. 14), and its T dependence will presumably become weaker as V_d increases. A possible explanation for the temperature dependence of F in Fig. 14 is that as the temperature becomes higher, thermal energy makes the space-charge limiting less effective. For example, in the case of a vacuum-tube diode, F is an increasing function of the cathode temperature [45]. However, further measurements at higher V_d, including the saturation region [18], and at lower T are definitely needed to be sure and for reliable cryogenic device modeling. Simulation with physical modeling, taking Coulomb interaction and the Pauli exclusion principle into consideration, will also be a powerful tool for further study [48,50].

The lowest temperature for noise characterization in this study was limited to 120 K because bipolar transistors were adopted in the LNA. The measurement method proposed here should be applicable down to 4 K by using an LNA composed of MOSFETs or GaAs high electron mobility transistors (HEMTs).

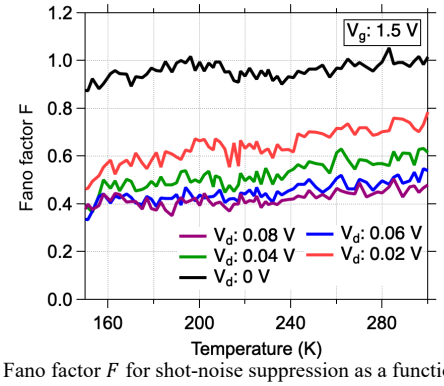

Fig. 14. Fano factor F for shot-noise suppression as a function of T at V_d ranging from 0 to 0.08 V.

IV. Conclusions

We have demonstrated variable-temperature characterization of N-MOSFETs, using the precisely calibrated PCB vehicle for broadband noise measurements from the flicker noise region to the white noise region. In order to build physics-based predictive models for MOSFETs, actual temperature-dependent measurements of broadband noise are necessary. Our measurement data show that a cryogenic environment reduces white noise at $V_\mathrm{d} = 0$ V as expected, but does not reduce shot noise that much at $V_\mathrm{d} \neq 0$ V. The latter will be a problematic noise source for applications in need of low-noise CMOS circuits.

Acknowledgment

The authors gratefully acknowledge the cooperative research with Prof. R. Hasunuma of University of Tsukuba.

References

[1] S. Takagi, A. Toriumi, M. Iwase, and H. Tango, "On the universality of inversion layer mobility in Si MOSFET's: Part I–Effects of substrate impurity concentration," *IEEE Trans. Electron Devices,* vol. 41, no. 12, pp. 2357–2362, Dec. 1994.

[2] Y.-W. Yi, K. Masu, K. Tsubouchi, N. Mikoshiba, "Temperature-scaling theory for low-temperature-operated MOSFET with deep-submicron channel," *Jpn. J. Appl. Phys.*, vol. 27, no. 10, p. L1958-L1961, Oct. 1988.

[3] H. L. Chiang, T. C. Chen, J. F. Wang, S. Mukhopadhyay, W. K. Lee, C. L. Chen, W. S. Khwa, B. Pulicherla, P. J. Liao, K. W. Su, K. F. Yu, T. Wang, H.-S. P. Wong, C. H. Diaz, J. Cai, "Cold CMOS as a power-performance-reliability booster for advanced FinFETs," *Symp. VLSI Technol., 2020*, pp. 1-2, doi: 10.1109/VLSITechnology18217.2020.9265065.

[4] Y. Nakamura, Y. A. Pashkin, T. Yamamoto, and J. S. Tsai, "Charge echo in a Cooper-pair box," *Phys. Rev. Lett.*, vol. 88, no. 4, p. 047901, Nov. 2016.

[5] Y. Nakamura, C. D. Chen, and J. S. Tsai, "Spectroscopy of energy-level splitting between two macroscopic quantum states of charge coherently superposed by Josephson coupling," *Phys. Rev. Lett.*, vol. 117, no. 19, pp. 2328–2331, Jan. 2002.

[6] D. Sank, Z. Chen, M. Khezri, J. Kelly, R. Barends, B. Campbell, Y. Chen, B. Chiaro, A. Dunsworth, A. Fowler, E. Jeffrey, E. Lucero, A. Megrant, J. Mutus, M. Neeley, C. Neill, P. J. J. O'Malley, C. Quintana, P. Roushan, A. Vainsencher, T. White, J. Wenner, A. N. Korotkov, and J. M. Martinis, "Measurement-induced state transitions in a superconducting qubit: Beyond the rotating wave approximation," *Phys. Rev. Lett.*, vol. 117, no. 19, 190503, Nov. 2016.

[7] P. Scarlino, D. J. van Woerkom, A. Stockklauser, J. V. Koski, M. C. Collodo, S. Gasparinetti, C. Reichl, W. Wegscheider, T. Ihn, K. Ensslin, and A. Wallraff, "All-microwave control and dispersive readout of gate-defined quantum dot qubits in circuit quantum electrodynamics," *Phys. Rev. Lett.*, vol. 122, no. 20, 206802, May 2019.

[8] M. Mehrpoo, B. Patra, J. Gong, P. A. 't Hart, J. P. G. van Dijk, H. Homulle, G. Kiene, A. Vladimirescuy, F. Sebastiano, E. Charbon, M. Babaie, "Benefits and challenges of designing cryogenic CMOS RF circuits for quantum computers," *International Symposium on Circuits and Systems*, May 2019.

[9] F. Sebastiano, H. Homulle, B. Patra, R. Incandela, J. van Dijk, L. Song, M. Babaie, A. Vladimirescu, E. Charbon, "Cryo-CMOS electronic control for scalable quantum computing," *54th Annual Design Automation Conference*, pp. 1–6, Jun. 2017.

[10] E. Charbon, M. Babaie, A. Vladimirescu, and F. Sebastiano, "Cryogenic CMOS circuits and systems–Challenges and opportunities in designing the electronic interface for quantum processors," *IEEE Microwave Magazine. Electron Devices*, vol. 22, no. 1, pp. 66–78, Jan. 2021.

[11] J. C. Bardin, D. H. Slichter, and D. J. Reilly, "Microwaves in quantum computing," *IEEE J. Microwaves*, vol. 1, no. 1, pp. 403–427, Jan. 2021.

[12] A. Beckers, F. Jazaeri, and C. Enz, "Theoretical limit of low Temperature subthreshold swing in field-effect transistors," *IEEE. Electron Device Lett.*, vol. 41, no. 2, pp. 276–279, Feb. 2020.

[13] P. A. 't Hart, M. Babaie, E. Charbon, A. Vladimirescu, and F. Sebastiano,"Characterization and modeling of mismatch in cryo-CMOS," *J. Electron Device Society*, vol. 8, pp. 263–273, Feb. 2020.

[14] A. Beckers, F. Jazaeri, and C. Enz, "Characterization and modeling of 28-nm bulk CMOS technology down to 4.2 K," *J. Electron Device Society*, vol. 6, pp. 1007–1018, Mar. 2018.

[15] R. Landauer, "Solid-state shot noise," *Phys. Rev. B*, vol. 47, pp. 16427–16432, June 1993.

[16] R. Sarpeshkar, T. Delbrück, and C. A. Mead, "White noise in MOS transistors and resistors," *IEEE Circuits Devices Mag.*, vol. 9, no. 6, pp.

23–29, Nov. 1993.
[17] R. Navid, C. Jungemann, T. H. Lee and R. W. Dutton, "High-frequency noise in nanoscale metal oxide semiconductor field effect transistors," *J. Appl. Phys.*, vol. 101, no. 12, p. 124501, Jun. 2007.
[18] K. Ohmori and S. Amakawa, "Direct white noise characterization of short-channel MOSFETs," *IEEE Trans. Electron Devices*, vol. 68, no. 4, pp. 1478–1482, Apr. 2021.
[19] J. Chen, Z. S. He, D. Kuylenstierna, T. Eriksson, M. Hörberg, T. Emanuelsson, T. Swahn, and H. Zirath, "Does LO noise floor limit performance in multi-gigabit millimeter-wave communication," *IEEE Microwave Compon. Lett.*, vol. 27, no. 8, pp. 769–771, Aug. 2017.
[20] J. Chen, D. Kuylenstierna, S. E. Gunnarsson, Z. S. He, T. Eriksson, T. Swahn, and H. Zirath, "Influence of white LO noise on wideband communication," *IEEE Trans. Microwave Theory Tech.*, vol. 66, no. 7, pp. 3349–3359, July 2018.
[21] Keysight Technologies, "Fundamentals of RF and microwave noise figure measurements," *Application Note*, 5952-8255E, 2019.
[22] L. F. Tiemeijer, R. J. Havens, R. de Kort, and A. J. Scholten, "Improved Y-factor method for wide-band on-wafer noise-parameter measurements," *IEEE Trans. Microwave Theory Tech*., vol. 53, no. 9, pp. 2917–2925, Sep. 2005.
[23] A. Sheldon, L. Belostotski, H. Mani, C. E. Groppi, and K. F. Warnick, "Cryogenic noise-parameter measurements—Recent research and a fully automated measurement application," *IEEE Microw. Mag.*, vol. 12, no. 8, pp. 52–64, Aug. 2021.
[24] A. Çağlar and M. B. Yelten, "Design of cryogenic LNAs for high linearity in space applications," *IEEE Trans. Circuits Syst. I*, vol. 66, no. 12, pp. 4619–4627, Dec. 2019.
[25] R. Hu and S. Weinreb, "A novel wide-band noise-parameter measurement method and its cryogenic application," *IEEE Trans. Microw. Theory Tech.*, vol. 52, no. 5, pp. 1498–1507, May 2004.
[26] K. Ohmori, R. Hasunuma, W. Feng, and K. Yamada, "Continuous characterization of MOSFET from low-frequency noise to thermal noise using a novel measurement system up to 100 MHz," *Symp. VLSI Technol.*, 2012, pp. 143–144.
[27] K. Ohmori, R. Hasunuma, S. Yamamoto, Y. Tamura, H. Jiang, N. Ishihara, K. Masu, and K. Yamada, "Application of low-noise TIA ICs for novel sensing of MOSFET noise up to the GHz region," *Symp. VLSI Circuits*, 2013, pp. C40–41.
[28] *Entrope Noise Probe*, https://www.devicelab.co.jp
[29] K. Ohmori and S. Amakawa, "White noise characterization of N-MOSFETs for physics-based cryogenic device modeling," *Electron Devices Technology and Manufacturing Conference*, 2021, pp. 1–3, doi: 10.1109/EDTM50988.2021.9420837.
[30] S. D. dos Santos, B. Cretu, V. Strobel, J.-M. Routoure, R. Carin, J.A. Martino, M. Aoulaiche, M. Jurczak, E. Simoen, C. Claey, "Low-frequency noise assessment in advanced UTBOX SOI nMOSFETs with different gate dielectrics," *Solid-State Electronics*, vol. 97, pp. 14–22, Jul. 2014.
[31] D. C. Murray, A. G. R. Evans, and J. C. Carter, "Shallow defects responsible for GR noise in MOSFET's," *IEEE Trans. Electron Devices*, vol. 38, no. 2, pp. 407–416, Feb. 1991.
[32] F. Yan, J. Bylander, S. Gustavsson, F. Yoshihara, K. Harrabi, D. G. Cory, T. P. Orlando, Y. Nakamura, J.-S. Tsai, and W. D. Oliver, "Spectroscopy of low-frequency noise and its temperature dependence in a superconducting qubit," *Phys. Rev. Lett.*, vol. 85, no. 17, p. 174521, May 2012.
[33] H. Achour, B. Cretu, E. Simoen, J.-M. Routoure, R. Carin, A. Benfdila, M. Aoulaiche, and C. Claeys, "Identification of Si film traps in p-channel SOI FinFETs using low temperature noise spectroscopy," *Solid-State Electron.*, vol 112, pp. 1–6, Oct. 2015.
[34] K. Ohmori, A. Shinoda, K. Kawai, Z. Wei, T. Mikawa, and R. Hasunuma, "Reduction of cycle-to-cycle variability in ReRAM by filamentary refresh," in *Proc. Symp. VLSI Technol.*, 2017, pp. T90–91.
[35] Keysight Technologies, "Using noise floor extension in an X-series signal analyzer," *Application Note*, 5990-5340EN, 2019.
[36] G. Ghibaudo. O. Roux, C. Nguyen-Duc, F. Balestra, and J. Brini, "Improved analysis of low frequency noise in field-effect MOS transistors," *Phys. Stat. Sol. (a)*, vol. 124, no. 2, pp. 571-581, Apr. 1991.
[37] L. K. J. Vandamme and F. N. Hooge, "What do we certainly know about 1/*f* noise in MOSTs," *IEEE Trans. Electron Devices*, vol. 55, no. 11, pp. 3070–3085, Nov. 2008.
[38] N. Apsley and H. P. Hughes, "Temperature- and field-dependence of hopping conduction in disordered systems," *Philosophical Magazine*, vol. 30, no. 5, pp. 963-972, 1974.
[39] R. Jayaraman and C. G. Sodini, "A 1/*f* noise technique to extract the oxide trap density near the conduction band edge of silicon," *IEEE Trans. Electron Devices,* vol. 36, no. 9, pp. 1773–1782, Sep. 1989.
[40] H. Achour, R. Talmat, B. Cretu, J.-M. Routoure, A. Benfdila, R. Carin, N. Collaert, E. Simoen, A. Mercha, C. Claey, "DC and low frequency noise performances of SOI p-FinFETs at very low temperature," *Solid-State Electron.*, vol 90, pp. 160–165, July 2013.
[41] R. Hettiarachchi, T. Matsuki, W. Feng, K. Yamada, and K. Ohmori, "Behavior of low-frequency noise in n-channel metal–oxide–semiconductor field-effect transistors for different impurity concentrations," *Jpn. J. Appl. Phys.*, vol. 50, no. 10S, p. 10PB04, Oct. 2011.
[42] M. J. Kirton and M. J. Uren, "Noise in solid-state microstructures: A new perspective on individual defects, interface states and low-frequency (1/f) noise," *Advances in Physics*, vol 38, no. 4, pp. 367–468, 1989.
[43] F. Yoshihara, K. Harrabi, A. O. Niskanen, Y. Nakamura, and J. S. Tsai, "Decoherence of flux qubits due to 1/f flux noise," *Phys. Rev. Lett.*, vol. 97, no. 16, p. 167001, Oct. 2006.
[44] A. van der Ziel, *Noise in Solid State Devices and Circuits.* New York, NY, USA: John Wiley & Sons, Inc., 1986.
[45] A. Ambrózy, *Electronic Noise*, McGraw-Hill, 1982.
[46] L. Chua, "Resistance switching memories are memristors," *Appl. Phys. A*, vol. 102, pp. 765–783, Mar. 2011.
[47] A. Rahman, J. Guo, S. Datta, and M. S. Lundstrom, "Theory of ballistic nanotransistors," *IEEE Trans. Electron Devices*, vol. 50, no. 9, pp. 1853–1864, Sep. 2003.
[48] N. Sano, K. Natori, K. Matsuzawa, and M. Mukai, "Current fluctuation characteristic of sub-0.1 micron device structures: a Monte Carlo study," *Jpn. J. Appl. Phys.*, vol. 38, no. 5A, pp. L531–533, May 1999.
[49] U. Fano, "Ionization yield of radiations. II. The fluctuations of the number of ions," *Phys. Rev.*, vol. 72, no. 1, pp. 26–29, July 1947.
[50] X. Chen, C. H. Chen, and R Lee, "Fast evaluation of the high-frequency channel noise in nanoscale MOSFETs," *IEEE Trans. Electron Devices*, vol. 65, no. 4, pp. 1502–1509, Apr. 2018.
[51] G. Iannaccone, A. Betti, G. Fiori, "Suppressed and enhanced shot noise in one dimensional field-effect transistors," *J. Comput. Electron.*, vol. 14, pp. 94–104, Feb. 2015.